Journal of the Geological Survey of Brazil

Inference of minerals at Redondão kimberlite crater, Parnaíba Basin, Brazil, based on interpretation of airborne gamma-ray spectrometry and ASTER data

Adolfo Barbosa da Silva[1*]

[1]Geological Survey of Brazil, Rua 148, 485, Setor Marista, Goiânia-GO, Brazil, CEP: 74170-110

Abstract

This work reports how minerals at Redondão kimberlite pipe may be inferred through the integrated interpretation of airborne gamma-ray spectrometry data and multispectral images derived from Advanced Spaceborne Thermal Emission and Reflection Radiometer (ASTER). Using several processing techniques (e.g., K, eTh, and eU concentration maps; K/eTh, K/eU, and eU/eTh ratio maps; K image inverse map; profile analysis for radiometric data; and spectral indexes and mineral distribution and abundance maps for ASTER data), it was observed that K concentrations within Redondão kimberlite intrusion are high enough to be distinct from the surroundings and at least three spectral signatures of endmembers extracted from ASTER images suggest that chlorite, diopside, and phlogopite minerals may be present within Redondão kimberlite crater and the near surroundings. Although the sources of K concentrations are unclear, they are probably composed of different minerals, including phlogopite. The spectral signatures of chlorite, diopside, phlogopite may be derived from clastic materials and products derived from weathered ultramafic mineral, but new studies are recommended to improve the distribution and abundance maps of these minerals. These new studies may include hyperspectral sensor images and rock-spectra data. The results reported here will be useful for further research whose goal is to map kimberlites using remotely sensed images not only in the study area, but also in other locations with similar geologic context.

Article Information

Publication type: Research Papers
Received 31 August 2023
Accepted 4 January 2024
Online pub. 8 January 2024
Editor: Vladimir Medeiros

Keywords:
Remote sensing
Advanced spectral analysis
Radiometric data
K-bearing minerals
Kimberlitic minerals
Mafic intrusions

*Corresponding author
Adolfo Barbosa da Silva
E-mail address: adolfo.barbosa@sgb.gov.br

1. Introduction

Kimberlites are ultrabasic rocks rich in volatiles and MgO whose magmas rise from great depths to the Earth's surface, carrying a set of crustal and/or mantle-derived xenoliths and xenocrystals, such that olivine, garnet, spinel, chromium-diopside, phlogopite, and diamond (Jelsma et al. 2009; Sparks 2013; Tappe et al. 2018; Woodhead et al. 2019). For this reason, in addition to being the primary source of a valuable mineral resource (diamonds), kimberlite studies provide an opportunity to investigate the chemical composition of the Earth mantle (Torsvik et al. 2010; Mitchell 2021).

The Brazil Diamond Project has mapped around 40 kimberlitic fields with 1365 cataloged intrusions (Silveira et al. 2018). The first intrusion was identified in 1965, but its kimberlitic affinity was only recognized in 1977. This intrusion was named Redondão kimberlite (Castelo Branco and Svisero 1986; Melo and Porto 1965 apud Svisero et al. 1977).

The Redondão kimberlite is an intrusion located c.a. 60 km from Alto Parnaba city, on the southern edge of the Parnaba Basin, in northern Brazil (Fig. 1). Redondão kimberlite occurs intruding Piauí and Pedra de Fogo formations sandstones near the Transbrasiliano Lineament (TBL) systems (Fig. 1b). Morphologically, this intrusion is an 80 m-deep crater bounded by an external ring with a 1 km-diameter semicircular shape (Figs. 2a and 2b). It is believed that this ring resulted from the differential erosion of silicified sandstones (Correia 1990) (Fig. 2c). The volcanic crater is filled by redeposited volcanic-sedimentary rocks with varying proportions of mineral fragments, such as altered olivine grain, olivine pseudomorphs, chloritized phlogopite, serpentine, saponite, talc, garnet, ilmenite, pyroxenite, chromite, zircon and terrigenous mixtures of sand and quartz (Castelo Branco and Svisero 1986; Correia 1990; Kaminsky et al. 2009).

Although the Redondão kimberlite occurs in a region where diamond occurrences have been documented (Svisero 1995; Oliveira 1998), research has indicated that tectonic positioning, geochemical characteristics and indicator mineral composition are key factors that make Redondão kimberlite unlikely to be economically viable

ISSN: 2595-1939
https://doi.org/10.29396/jgsb.2024.v7.n1.2
Open access at https://jgsb.sgb.gov.br/index.php/journal

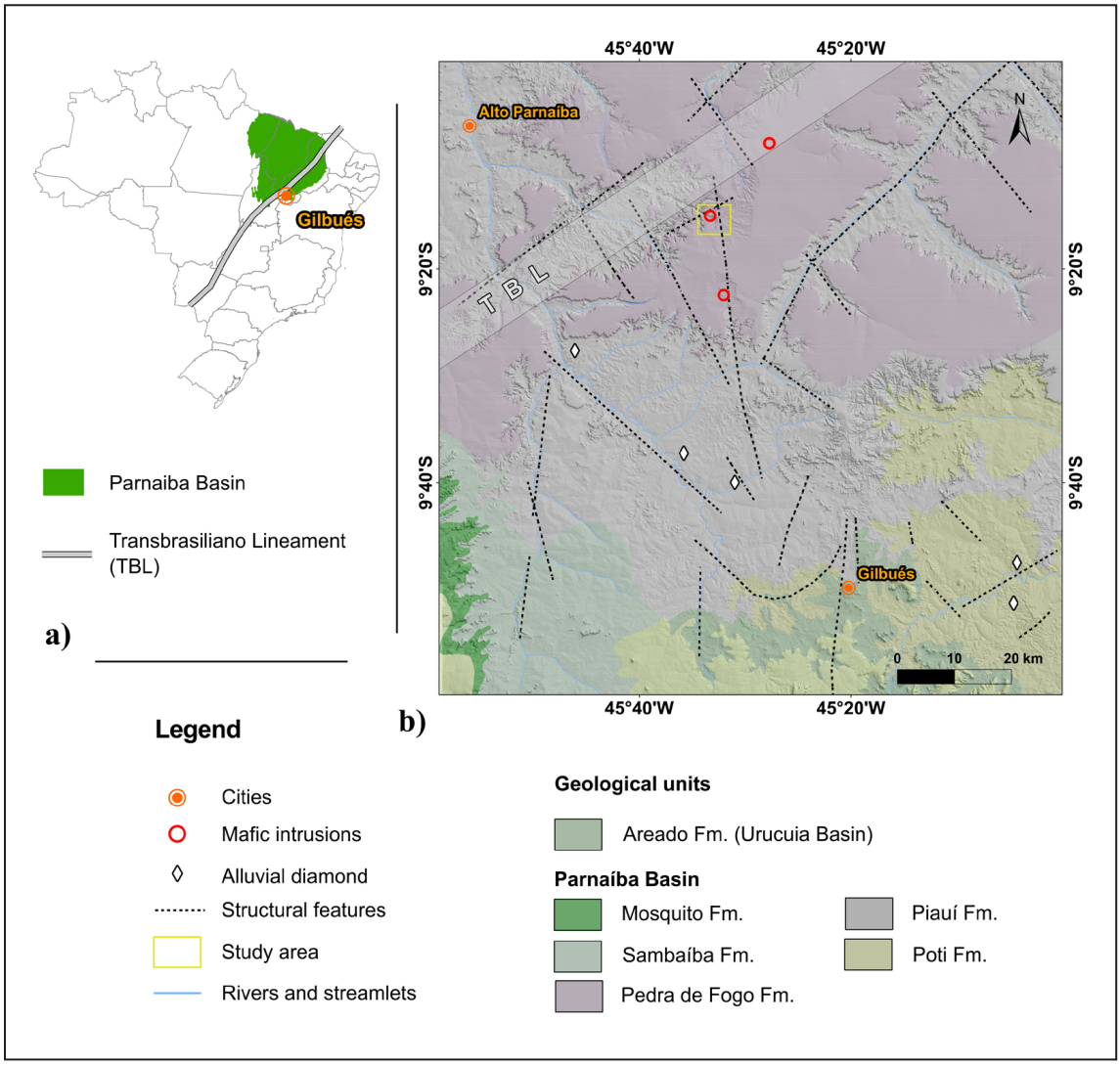

FIGURE 1. Regional geological map of the study area. The location of structural features and occurrences of alluvial diamonds was digitized from Correia (1990). The geological units were obtained through the GeoSGB portal (https://geosgb.sgb.gov.br/).

(Correia 1990; Kaminsky et al. 2009). On the other hand, these alluvial diamonds may derive from other kimberlitic intrusions that have not been mapped yet (Correia 1990). In this context, analysis of data from remote sensors (such as airborne geophysics and satellite images) can be useful tools in the task of mapping new kimberlitic intrusions (Tessema et al. 2012; Reed and Witherly 2007).

Previous works have demonstrated that indicator minerals of kimberlitic intrusions, such as olivine, chromium-diopside, enstatite, serpentine and phlogopite, may have their respective spectral signatures detected by multispectral images (Tessema et al. 2012; Nndanduleni and Tessema 2021; Guha et al. 2015). Although magnetic and electromagnetic data are commonly used to map kimberlites (Macnae 1995; Pettit 2009; Menezes and La Terra 2011; Kaminski and Oldenburg 2012; Tessema et al. 2012; Nndanduleni and Tessema 2021; Matende and Mickus 2021), analysis of airborne gamma-ray spectrometry (AGRS) data can also contribute to reveal the presence of kimberlite-related minerals or to indicate areas where processes related to the formation and alteration of the kimberlitic crater may have occurred (Killeen et al. 2015; Mwenifumbo and Kjarsgaard 1999; Yakovlev 2020).

At Redondão kimberlite intrusion, interpretations of gamma-ray and spectral signatures of kimberlites based on remotely sensed images have been little addressed and there are few studies published that make an integrated interpretation of the images generated by the different sensors (e.g., radar, Landsat-TM, and aerial photographs) (Castelo Branco and Svisero 1986; Lima et al. 1990; Almeida-Filho and Castelo Branco 1992). Aiming to fill this knowledge gap, this work has the prime objective of inferring the presence of minerals at Redondão kimberlite pipe through the integrated interpretation of airborne gamma-ray spectrometry data and multispectral images derived from Advanced Spaceborne Thermal Emission and Reflection Radiometer (ASTER). Using several processing techniques, it is proposed that chlorite, diopside, and phlogopite minerals may explain the main findings of this study. These results can be useful for further research whose goal is to map kimberlites using remotely sensed images not only in the study area but also in other places with similar geological contexts.

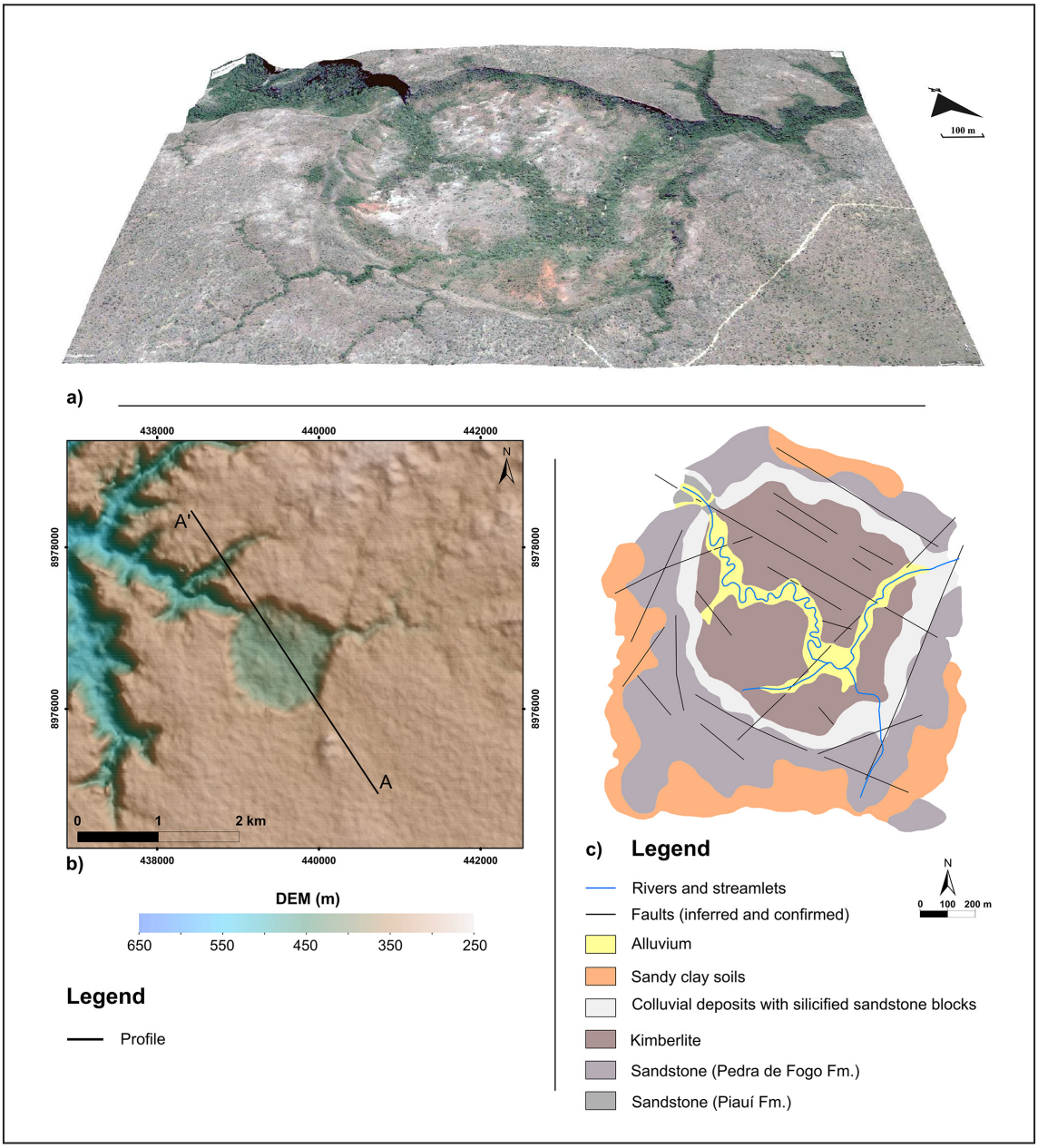

FIGURE 2. Details of the Redondão kimberlite intrusion. a) 3D view of the kimberlitic crater. Image obtained through the Google Earth platform on June 5, 2022. b) Elevation map of the study area. The A – A' profile is described in the text. c) Simplified Redondão kimberlite geological map. Modified from Correia (1990).

2. Materials and methods

2.1 Airborne gamma-ray spectrometry and ASTER satellite database

The AGRS data processed and interpreted in this study was acquired and pre-processed in 2005/2006 by Atech/USP and is in the domain of the Petroleum, Natural Gas and Biofuels Agency. They were acquired along the flight with a 500 m-spacing and a 100 m clearance terrain height. Gamma-ray measurements were recorded using a gamma-spectrometer with sodium iodide (NaI) crystal detectors whose measurements were taken every 1.0s. The AGRS database is available on the REATE platform upon code 0050_MAGGAMA002 (https://reate.cprm.gov.br/anp/TERRESTRE) and the following corrections have been made: dead time, background removal (aircraft, cosmic and radon), height, and the Compton Effect (Marques et al. 2007).

The ASTER sensor comprises three radiometers onboard the Terra satellite that, together, capture solar radiation reflected and emitted by the Earth's surface in three regions of the electromagnetic spectrum (Yamaguchi et al. 1998): visible and near infrared (VNIR); shortwave infrared (SWIR); and thermal infrared (TIR). These regions are divided into 14 spectral bands with spatial resolutions of 15 m, 30 m and 90 m for the VNIR, SWIR and TIR bands, respectively.

The ASTER images were generated on April 6, 2001 (ASTER granule ID = AST_L1T_00307042001133819_20150418064351_118591), pre-processed by the Land Processes (LP) Distributed Active Archive Center (DAAC) team, and later made available on the USGS Earth Explorer platform (LP DAAC 2020). The image processing level is L1T, which

includes radiometric, geometric, cross-talking, terrain accuracy and north rotation corrections (LP DAAC 2020). Scene data contains sensor calibrated radiance and cloud cover less than 2%.

The gamma-ray spectrometry data were processed using Seequent's Oasis Montaj software version 9.8.1, whereas ASTER images were processed using NV5 Geospatial's ENVI software version 5.6.2. Esri's ArcGis software version 10.6 was used to organize results into maps. More detailed descriptions of this data processing are given in the next sections.

2.2 Airborne gamma-ray spectrometry data processing

The K, eTh and eU channels from the AGRS database were interpolated by the inverse distance weighted method, with a 125-m cell size and a 500 m-search radius. The K, eTh and eU resulting grids were used to calculate the radiometric ratios, F- parameter (Fp), and RGB composite color images.

Calculating radioelement ratios is a useful tool to highlight subtle variations in the relative behavior of radioelements because it suppresses various effects that degrade the gamma signal, such as soil mixing and detector geometry (IAEA 2003; Killeen et al. 2015). During the airborne radiometric processing step, it was found that the highest K concentrations in the study area coincided with the location of the Redondão kimberlite pipe. In order to highlight these concentrations, this work has chosen to compute K/eTh and K/eU ratios. The eU/eTh ratio was also computed with the aim of investigating the behavior of the eU in relation to the eTh.

The K/eTh and K/eU ratios were also used to produce the K Inverse Image (IIK) (Duval 1983; Dentith and Mudge 2014). In this image, K concentrations and K/eTh and K/eU ratios are combined into an RGB composite color with K concentrations in the Red band, and K/eTh and K/eU ratios in the Green and Blue bands, respectively. In this composition, areas with high K concentration and with K enrichment relative to eTh and eU are expected to be seen in bright, whereas dark areas denote low K concentration in conjunction with relative enrichment of eTh and eU to K (Duval 1983).

Fp was computed by dividing K and eU products by eTh (Efimov 1978 apud Gnojek and Přichystal 1985). This also tends to attenuate the effects (soil mixtures, detector geometry, etc.) of gamma signals, and this factor can be interpreted as an altered rock index, especially with regard to the change that leaves K concentration (Gnojek and Přichystal 1985). Overall, Fp values less than 1.3 x 10^{-2} are interpreted as indicative of common non-altered rocks, whereas Fp values greater than 2 x 10^{-2} or even 5 x 10^{-2} (exceptionally 10) are interpreted as indicative of altered rocks (Efimov 1978 apud Gnojek and Přichystal 1985).

All radiometric themes aforementioned were organized into maps superimposed on a hill shaded with 40% transparency. This hill shaded was computed from the Digital Elevation Model (DEM) with 30 m horizontal resolution, which was derived from the Shuttle Radar Topography Mission. A polygon representing the outline of the Redondão kimberlite crater has been added to facilitate interpretation. In addition to maps, the results of the gamma-ray spectrometry data processing were also organized into a profile. In this profile, radioelement concentrations, ratios, Fp, and DEM data were sampled with the same spacing (125 m) to a database corresponding to the direction of profile A – A' shown in figure 2b.

2.3 ASTER images processing

The ASTER L1T's VNIR and SWIR bands were calibrated and then atmospherically corrected using the QUIck Atmospheric Correction (QUAC). Following the observations of Guha and Kumar (2016), the atmospheric correction was not applied to TIR bands, as such corrections can insert artifacts into these bands and make them even noisier. Then the VNIR bands were resampled to a resolution of 30 m and stacked with the SWIR bands in a single multilayer raster (VNIR – SWIR).

After atmospheric correction, analysis of vegetation was performed to suppress vegetation spectral signatures in VNIR - SWIR and TIR scenes. This task was performed using the Otsu method applied to the Normalized Difference Vegetation Index (NDVI) image. This method can be used to separate two classes (e.g., pixels with and without vegetation effects) by discriminant analysis (Otsu 1979). After the analysis of vegetation, RGB composite color of spectral indices and mineral distribution and abundance maps were produced from the VNIR - SWIR and TIR images.

The following indices were calculated from the VNIR – SWIR raster: Clay Mineral Ratios (CMR), Ferrous Mineral Ratios (FMR), Iron Oxide Ratios (IOR) (Drury 2001; Kalinowski and Oliver 2004). The TIR bands were used to compute Quartz-bearing Rocks (QRI), Mafic mineral-bearing Rocks (MRI) and Feldspar-bearing Rocks (FRI) indices according to Guha and Kumar (2016)'s equations. The CMR, FMR and IOR indices were combined into an RGB image and organized into a map. The same procedure was performed for the indices derived from the TIR bands. Similar to the radiometric maps, the RGB spectral indices were overlaid on the DEM with a transparency of 40%.

The mineral distribution and abundance maps were produced by the Advanced Spectral Analysis (ASA) approach. To reduce the spectral influence of surrounding materials, this approach was applied at an area immediately near to Redondão kimberlite crater. In ASA approach, distribution and abundance maps were computed basically following three steps described at the next lines.

In the first step, a spectral dimensionality reduction was performed using the Minimum Noise Fraction (MNF) transformation and the results were used as an input parameter for the Pixel Pure Index (PPI) function (Green et al. 1988; Boardman et al. 1995; Van der Meer and De Jong 2000). This function allows identifying the most spectrally pure pixels present in the images, thus allowing the selection of endmembers. The PPI function was run with 8,000 interactions and a threshold value of 2.50. Subsequently, the spectra of the PPI image pixels were projected into an n – dimensional space (n - D visualization) and the endmembers were extracted manually by drawing regions of interest (ROI's) (Bateson and Curtiss 1996; Pal et al. 2011). For each endmember, it was considered the mean reflectance of the pixel group within each ROI (Pal et al. 2011).

After endmembers were extracted, they were identified in a second step. This was done by comparing endmember spectral with spectral mineral references derived from spectral library. This comparison was carried out by visual analysis and spectral ranking. Initially, based on the geological studies of previous works (Correia 1990; Kaminsky et al. 2009), this study selected eleven spectra (namely reference spectra)

whose minerals were mapped in the Redondão kimberlite crater: chlorite, diopside, magnetite, olivine, phlogopite, quartz, saponite, serpentinite, talc, zircon, and ilmenite. The reference spectra were obtained from USGS Spectral Library (Kokaly et al. 2017) and resampled for the ASTER sensor. Thereafter, endmember and reference spectra were compared by visual analysis and by ranking of spectral similarity.

To visually compare the spectra, a continuum curve was removed from reflectance values of both endmembers and references (Clark and Roush 1984) and the spectra were plotted on a graph. To build a ranking of spectral similarity, Spectral Mapping Angle (SAM), Spectral Feature Fitting (SFF), and Binary Encoding (BE) techniques were used (Pal et al. 2011). The SAM compares the spectral similarity between two spectra by calculating the angle between the spectra and treating them as vectors in a space with a dimension equal to the number of bands (Kruse et al. 1993). SFF is an absorption-feature-based technique that compares the fit of image spectra to a reference using a least-squares method (Clark et al. 1992; Clark et al. 1990; NV5 Geospatial 2023a), whereas the BE method encodes both endmember and reference spectra and uses Hamming distance to measure the similarities (Mazer et al. 1988; NV5 Geospatial 2023b). Each of these techniques returns a similarity measure whose values are combined into ranking or weighted scores. The scores range from 0 to 1; the closer to 1 indicates the closest match and indicates higher confidence in the spectral similarity.

After the step of comparing endmembers and reference spectra, the spectra identified were used to produce the mineral distribution and abundance maps. In addition, the SAM method, Mixture Tuned Matched Filtering (MTMF) was used to produce these maps. The MTMF uses partial unmixing to quantify the relative abundance of endmembers user-defined into the pixel image by maximizing the response of the known target endmember and suppressing the response of other materials from the unknown background (Boardman 1998; Girija and Mayappan 2019). Both SAM and MTMF techniques have been successful at mineral identification (Rowan and Mars 2003; Khan and Mahmood 2008; Kruse et al. 1993; Pal et al. 2011; Pour et al. 2015). For the mineral distribution maps, the SAM algorithm was run considering a maximum angle of 0.1 radians for all classes, that is, pixels with values greater than this limit were not classified. For MTMF, a background threshold of 0.9 was considered.

Commonly, MTMF score results are composed of Match Filter scores (MF score) and Infeasibility images. In the MF score, pixel values range from 0 to 1, and this range can be interpreted as the proportion of the pixel spectral at images that contain the spectral signature of the mineral under analysis (Girija and Mayappan 2019). In the MTMF score images, the closer to unity, the better the matching between the spectra from image and reference spectra (Girija and Mayappan 2019). On the other hand, infeasibility maps help to identify possible false positives. In the MTMF results, pixels with high MF score and infeasibility near 0 are the most reliable.

To facilitate the interpretation of MTMF maps, MF score and infeasibility images were reclassified. Pixels with MF score above 0.1 (that is, pixels whose spectral signatures contain at least 10% or more of the spectral signature target) were reclassified for a value equal to 1, and pixels with MF score values below 0.1 were considered to be zero. Contrarily, pixels with infeasibility values below 1.5 were reclassified for values equal to 1, whereas pixels with infeasibility values above 1.5 or more were considered to be zero. Then, each pixel of MF score reclassified image was multiplied by each pixel of the infeasibility reclassified image, so that only pixels with MF score > 0.1 and infeasibility < 1.5 had a value equal to 1 in the final image. The zero values were masked out. This procedure was done for each endmember identified. Finally, SAM and MTMF results were organized into maps.

3. Results

Figure 3 shows the radiometric concentration maps (K, eTh and eU) and the ratios (K/eTh, K/eU and eU/eTh). In the survey area, average concentration of K, eTh and eU are 0.18%, 7.96 ppm and 1.37 ppm, respectively. These average values suggest that the survey area is characterized by very low radiometric signatures. However, K concentrations of up to 0.47% occur in the inner portion of the KR and such concentrations can be clearly distinguished from the surrounding area (Fig. 3a).

In the maps of eTh and eU concentration as well as K/eU and eU/eTh ratio maps (Figs. 3b, 3c, 3e and 3f), at first, it is not possible to observe any radiometric feature within the crater boundary. On the other hand, there is a peak in the value of the K/eTh ratio also occurring in the inner portion (Fig. 3d) of the volcanic crater, more precisely in its central-eastern portion. The K and K/eTh maps suggest the existence of K enrichment mainly in relation to eTh.

In the IIK and Fp maps, the relative enrichment idea is reinforced. Figure 3a shows that the kimberlitic crater is marked by bright colors, revealing not only highlighted K concentration itself, but also that this concentration is relatively more enriched than eTh and eU. In the Fp map (Fig. 4b), while the surrounding area is characterized by low values ($Fp < 0.08 \times 10^{-2}$), areas with Fp up to 0.14×10^{-2} occur within the kimberlitic crater.

The K enrichment is also reinforced by the profile analysis results, which show that the K concentration curve reaches its maximum value just within the kimberlite crater (Fig. 5). The same occurs for the Fp curve (Fig. 5). As seen on the map, eU and eTh concentration curves do not show features that can be correlated with the crater shape. However, unlike what was observed on the eU/eTh map (Figs. 4e and 4f), K/eU and eU/eTh ratio curves can be correlated with the structure of the kimberlitic crater. For instance: maximum values of the K/eU and K/eTh ratio curves also occur in the crater center, coinciding with the maximum values of the K, Fp and eU/eTh concentration curves. The latter, however, has a more complex behavior, with other maximum values occurring outside the crater center. Two of them even appear to occur near the edges of kimberlitic crater.

The results of the vegetation analysis are shown in Figure 6. The RGB composite color VNIR – SWIR raster and NDVI map show that pixels with spectral signatures dominated by vegetation are strongly highlighted in red, mainly that near drainage channels (Figs. 6a and 6b). Based on the Otsu method, this study has considered that pixels with values greater than 0.463 on the NDVI image were considerably affected by vegetation and, therefore, were masked out from subsequent products. Figure 3c shows that the majority of pixels masked out occur near drainage channels, indicating that the analysis of vegetation was successful.

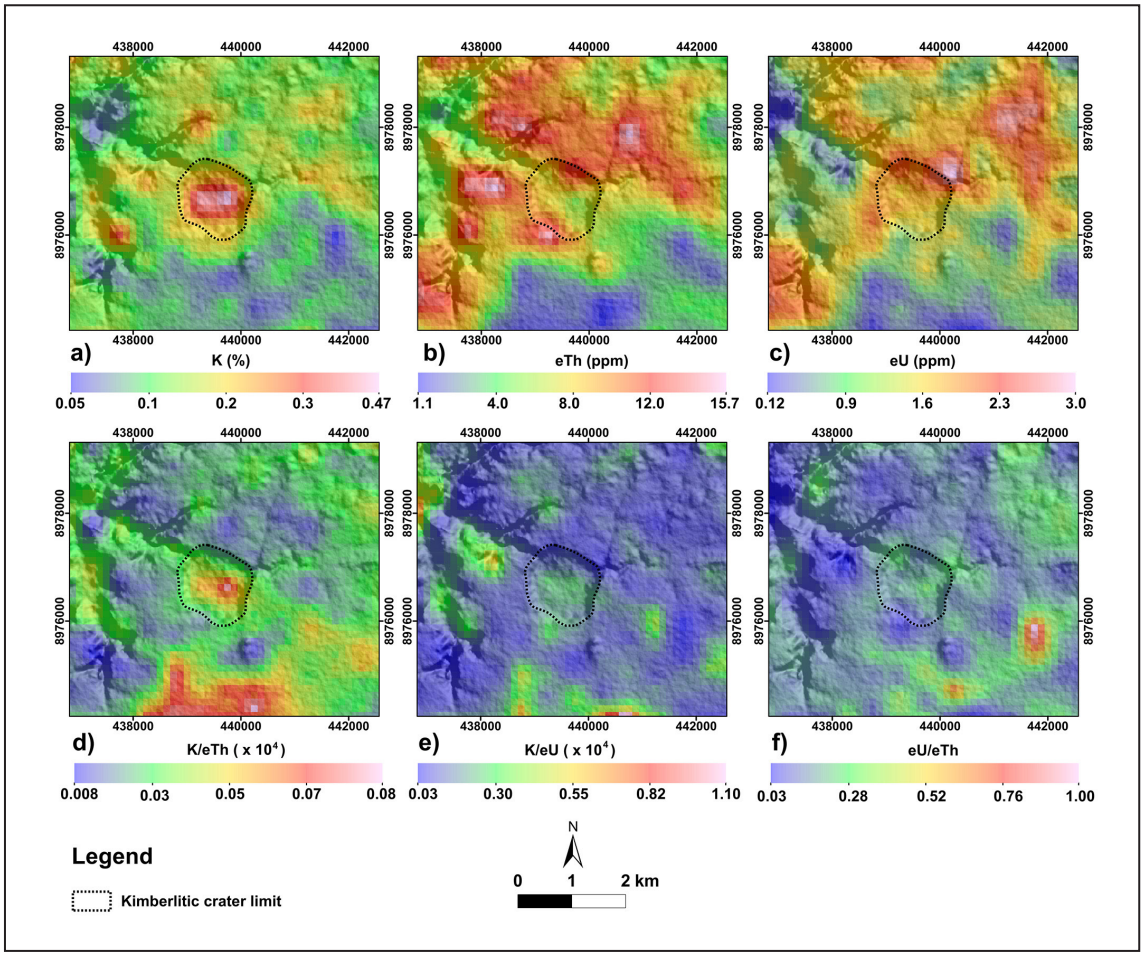

FIGURE 3. Thematic radiometric maps. a) K concentration. b) eTh concentration. c) eU concentration. d) K/eTh ratio. e) K/eU ratio. f) eU/eTh ratio. All maps were superimposed on the DEM with transparency of 40%.

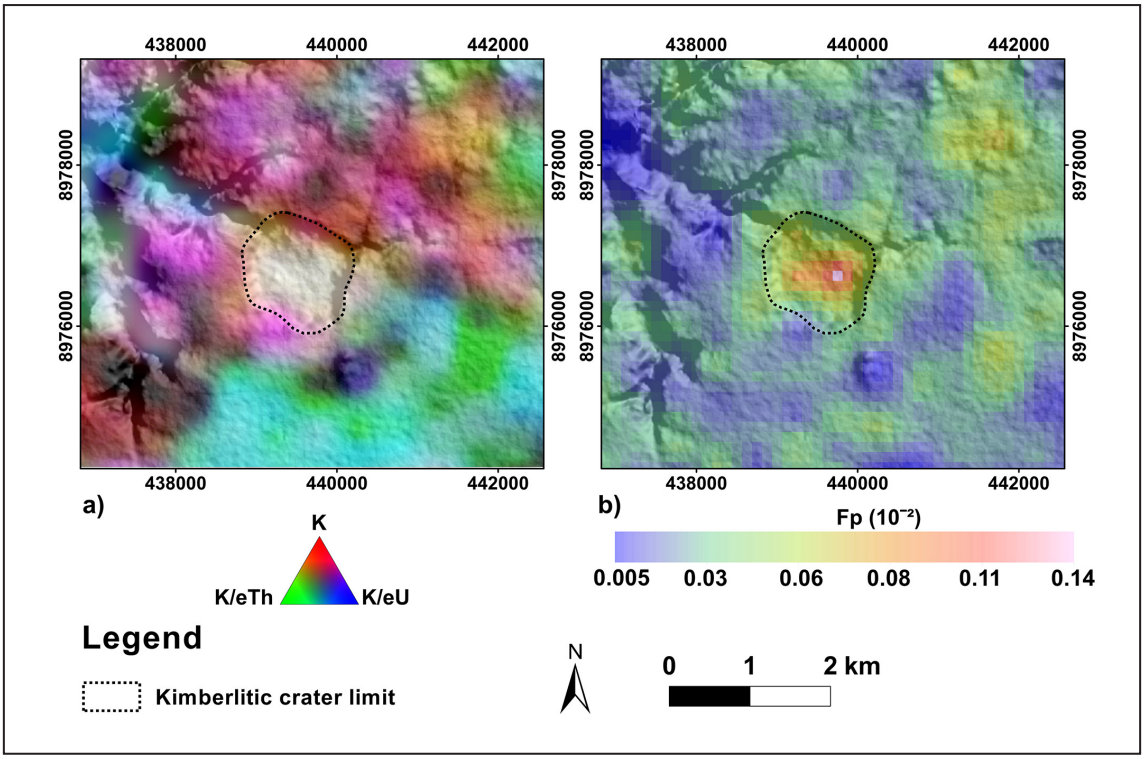

FIGURE 4. : Thematic radiometric maps. a) K Inverse Image (KII). b) F - parameter (Fp).

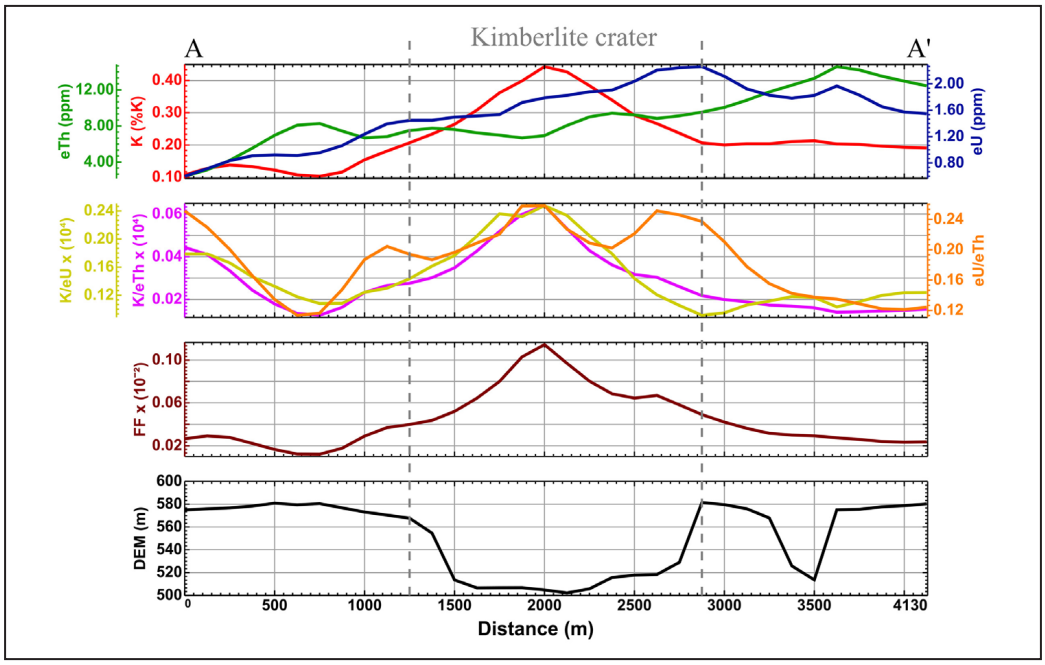

FIGURE 5. Profile A - A' showing concentration and ratio radiometric curves and Digital Elevation Model curve.

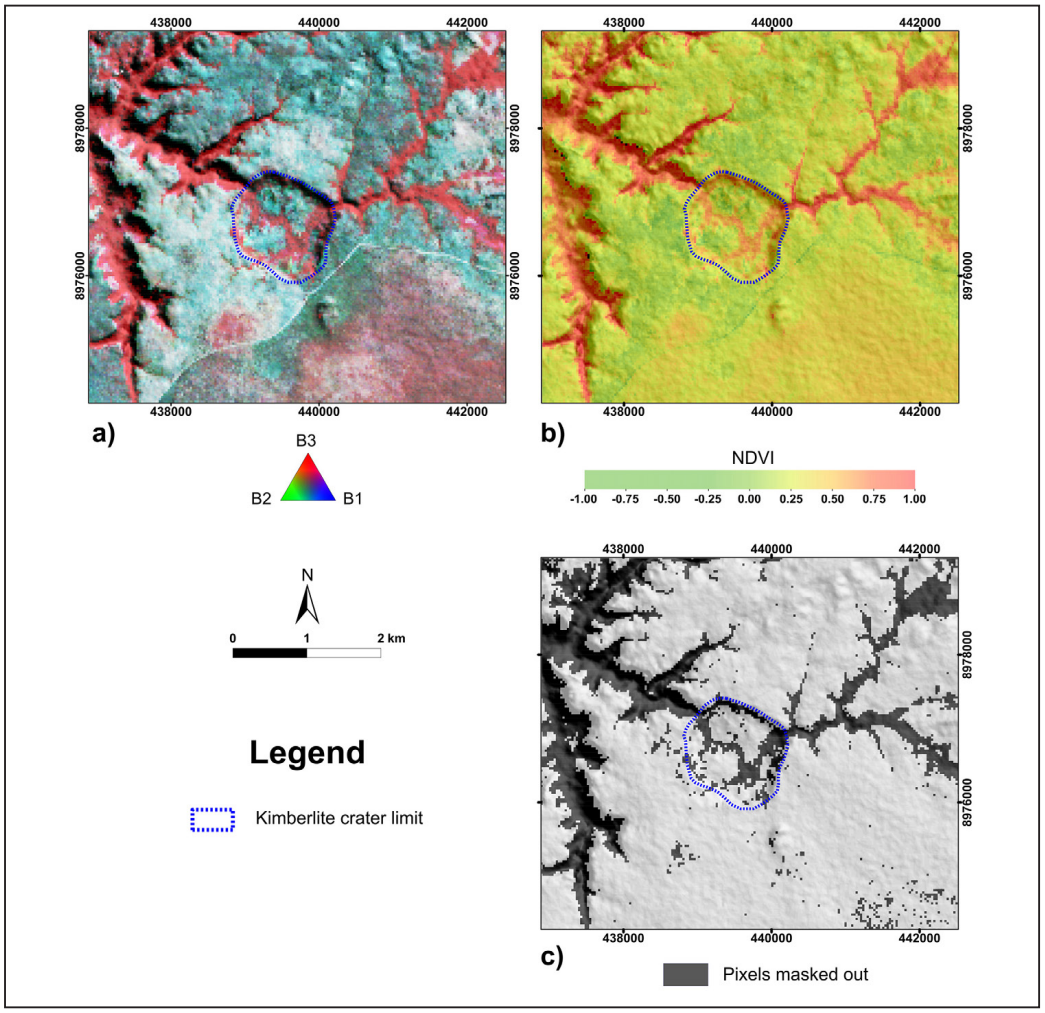

FIGURE 6. Vegetation analysis. a) RGB composite color of bands 3, 2, 1 of VNIR – SWIR raster. Vegetation is strongly highlighted in red. b) NDVI map. The highest values occur close to the drainage channels. c) Masked image created from NDVI. Masked-out pixels have an NDVI ≥ 0.463. All images with 40% transparency are superimposed on the Digital Elevation Model.

The RGB composite color for spectral indexes produced from VNIR - SWIR and TIR images are displayed at figure 7. In the figure 7a, reddish shades indicate clay minerals, and greenish and bluish shades indicate ferrous and iron ferric oxide minerals, respectively. Overall, results indicated clay minerals are abundant at the northwest and southeast study area. Clay minerals also occur near drainages, including those within kimberlite crater. On the other hand, Redondão kimberlite crater is characterized by a weak cyan/medium greenish shade, mainly in a little region at the southwest (see the black arrow in figure 7a), suggesting the presence of ferrous and iron ferric oxide minerals within the crater. However, the presence of ferrous and ferric iron oxide minerals seems to occur outside the crater.

Instead of spectral indexes VNIR - SWIR results, spectral indexes derived from TIR images yielded poor results in terms of resolution. Nevertheless, one can see that the little region aforementioned is seen as a strong blue shade in Figure 7a (compare the black arrow in Figure 7b), which suggests the presence of mafic silicate minerals. It means that the little region may contain Fe-bearing mafic silicate minerals. Again, these minerals may also be present outside the kimberlitic crater.

In MNF analysis, MNF bands with eigenvalues < 1 are considered to be dominated by noise (Fig. 8a). Although all eigenvalues were greater than unity, only the first four were above the break in the slope of the curve of the MNF eigenvalues chart (Fig. 8a). This means that most of the coherent signal is contained in the first four MNF bands. However, to avoid possible underestimation of dimensionality, this study chose to select the first five MNF bands. Thus, the 5-MNF band was considered as the boundary between coherent images and those dominated by noise (Fig. 8a).

The figures 8b and 8c show the set of pure pixels projected in n - dimensional space. To facilitate the presentation of results, three numbered axes were fixed. The axes numbers correspond to the first five MNF bands. After analysis of n - dimensional space, five endmembers located approximately at the vertices of the point cloud were selected (Van der Meer and De Jong 2000) (Figs. 8b and 8c). Among the five endmembers selected, only three (namely #1, #2, and #3) were identified by visual analysis and by ranking of spectral similarity. The two endmembers remaining were ruled out because their spectral signatures do not match any of the target spectra chosen in this study.

Figure 9 shows the spectra of these three endmembers compared to the chlorite, diopside, and phlogopite laboratory spectra. The results show that endmember #1 and chlorite spectra have absorption features at 0.66 µm, 0.88 µm, 2.26 µm, and 2.33 µm, but these features are pronounced at the chlorite spectral curve. The endmember #2 and diopside spectra have absorption features very similar in 0.66 µm, but 2.26 µm wavelengths are more clear and deepest in the diopside spectrum. Similarly, absorption features in 2.33 µm region are also clearer for the phlogopite reflectance curve than endmember #3. However, absorption features at 2.26 µm seem sharper for endmember #3 than phlogopite.

Table 1 shows the results for the ranking of spectral similarity. Besides the scores, this table shows mineral names and formulas. According to table 1, endmember #1 and chlorite spectra yield the highest score, meaning high similarity. High similarities were also verified for endmember #2/diopside

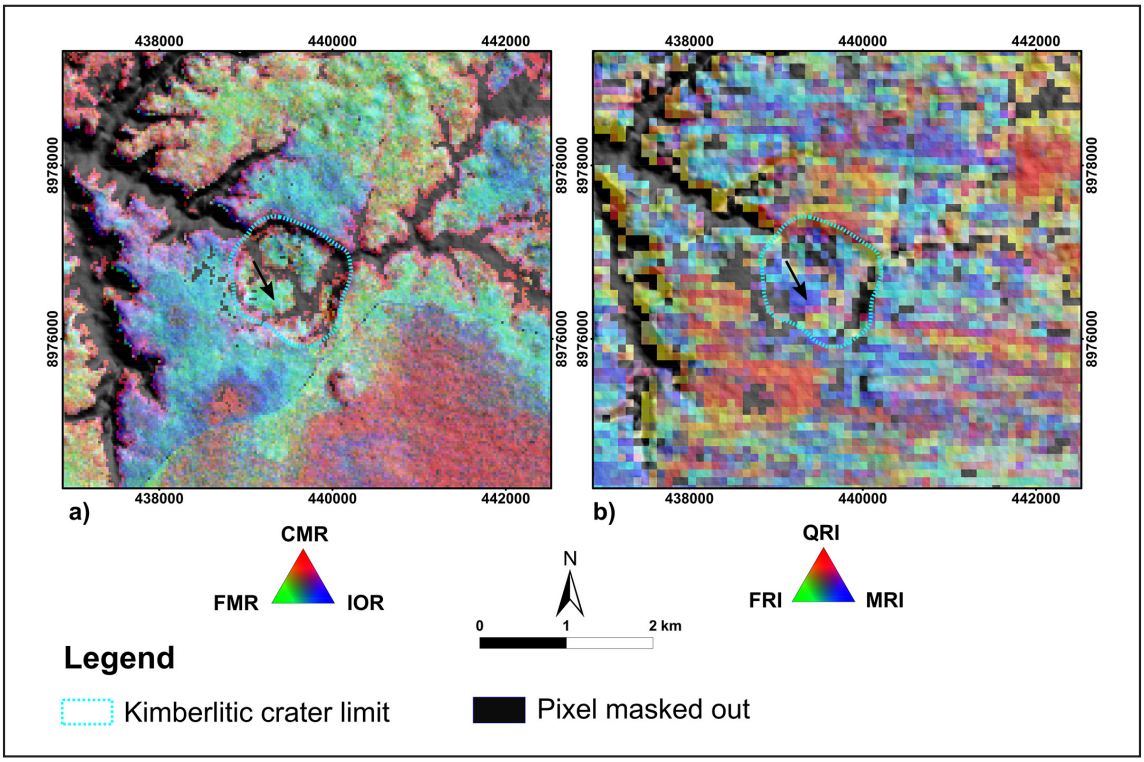

FIGURE 7. Color composition of spectral indices. a) RGB composite color of Clay Mineral Ratios (CMR), Ferrous Mineral Ratios (FMR), and Iron Oxides Ratios (IOR). b) RGB composite color of Quartz - bearing rock Index (QRI), Mafic mineral - bearing rocks index (MRI), and Feldspar - bearing rocks Index feldspar (FRI). The black arrow indicates a region may have contained Fe-bearing mafic silicate minerals within the kimberlite crater.

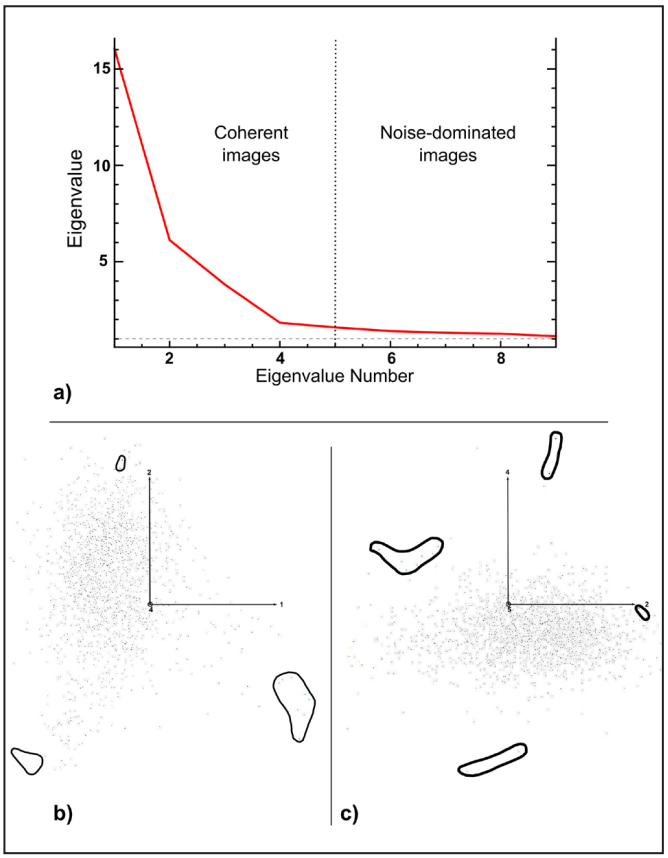

FIGURE 8. Advance spectral analysis results. a) MNF eigenvalues chart. The dotted straight line separates coherent and noise-dominated MNF bands. b) and c) Endmember identification at n-D visualization. Each polygon represents a Region of Interest (ROI) containing pure pixels. The numbers of axes represent MNF bands.

and endmember #3/phlogopite spectra. The visual analysis and ranking of spectral similarity results suggest that chlorite, diopside, and phlogopite spectra can be present in VNIR-SWIR images.

Figure 10 shows mineral distribution maps derived from SAM results. Figures 10a to 10c are images with the angular difference (in radians) between the VNIR - SWIR image pixel spectra and reference spectra (chlorite, diopside, or phlogopite). Figure 10d is the VNIR - SWIR image classified by SAM method.

Spatially, SAM results show the lowest angle differences can be seen for phlogopite and the largest for diopside, and both value classes occur within or outside the kimberlite crater (Figs. 10b and 10c). Low angle differences can also be seen for chlorite, but they are more frequent within kimberlite crater (Fig. 10a).

In the little region within the kimberlite crater where the spectral indices have suggested the presence of Fe-bearing mafic minerals, angular differences of c.a. 0.12 (or 6.87°), 0.2 (or ~11.46°), and 0.05 (or ~2.84°) can be seen for chlorite, diopside, and phlogopite (black arrow at Figs. 10a, 10b, and 10c). It means that when endmember and reference spectra are treated as vectors in this little region, they are very similar because the angle differences between them are less than 12 degrees.

Regarding the classified image, only the phlogopite class was identified. Probably, this has occurred because only pixels with angular differences less than 0.1 radians (or

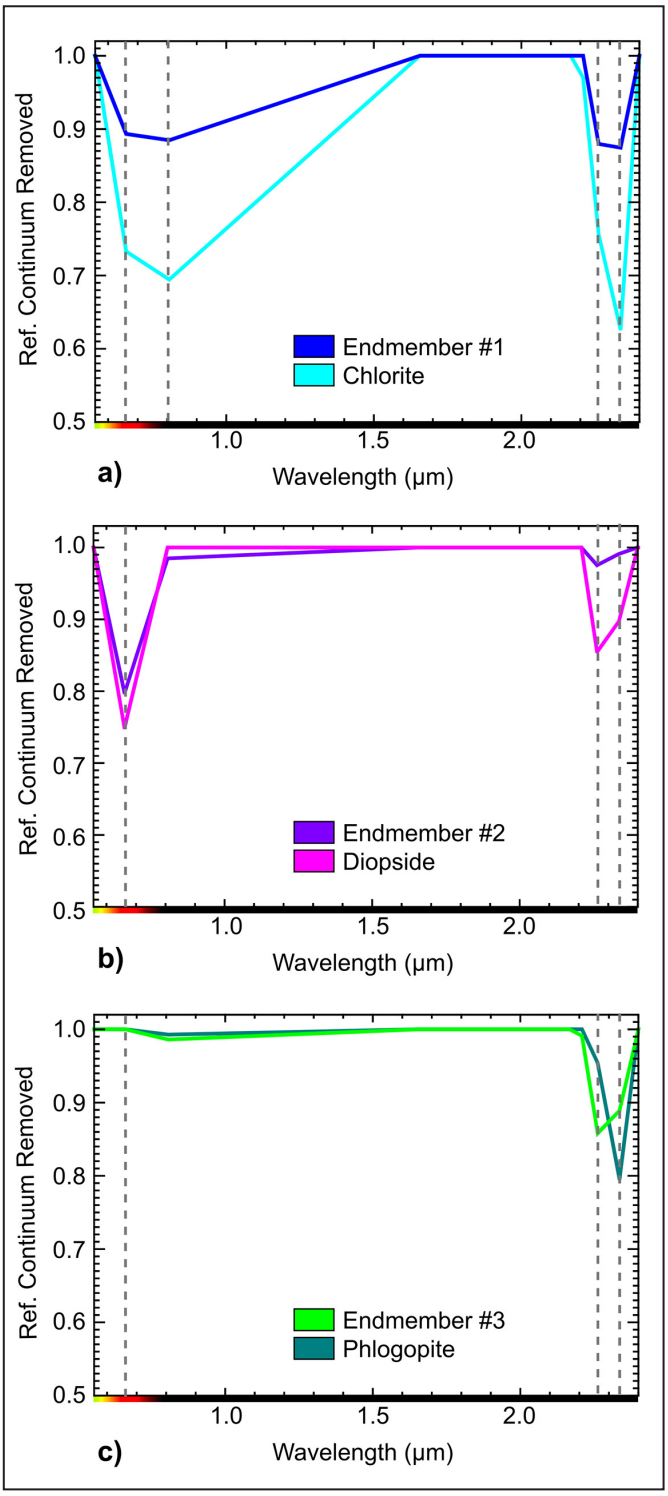

FIGURE 9. Visualization analysis of spectral profiles. a) Endmember #1 and chlorite comparison. b) Endmember #2 and diopside comparison. c) Endmember #3 and phlogopite comparison. The gray dotted straight line marks the main absorption features.

~5.73°) were classified in the final image. Notwithstanding, SAM results suggest that chlorite, diopside, and phlogopite may be at kimberlite crater, mainly in the aforementioned little region.

In Figure 10, each pixel with an MF score > 0.1 and infeasibility < 1.5 is labeled as MTMF class. This class, in turn, indicates what reference spectra (if chlorite, diopside, or phlogopite) best match the VNIR - SWIR image pixel

TABLE 1: Ranking of spectral similarity.

Endmember	Mineral	Formula	Scores			
			SAM	SFF	BE	Total
#1	Chlorite	(Mg,Fe)3(Si,Al)4O10(OH)2-(Mg,Fe)3(OH)6	0.79	0.89	1.00	2.68
#2	Diopside	CaMgSi2O6	0.73	0.51	0.89	2.13
#3	Phlogopite	KMg3Si3AlO10(F,OH)2	0.85	0.62	0.89	2.36

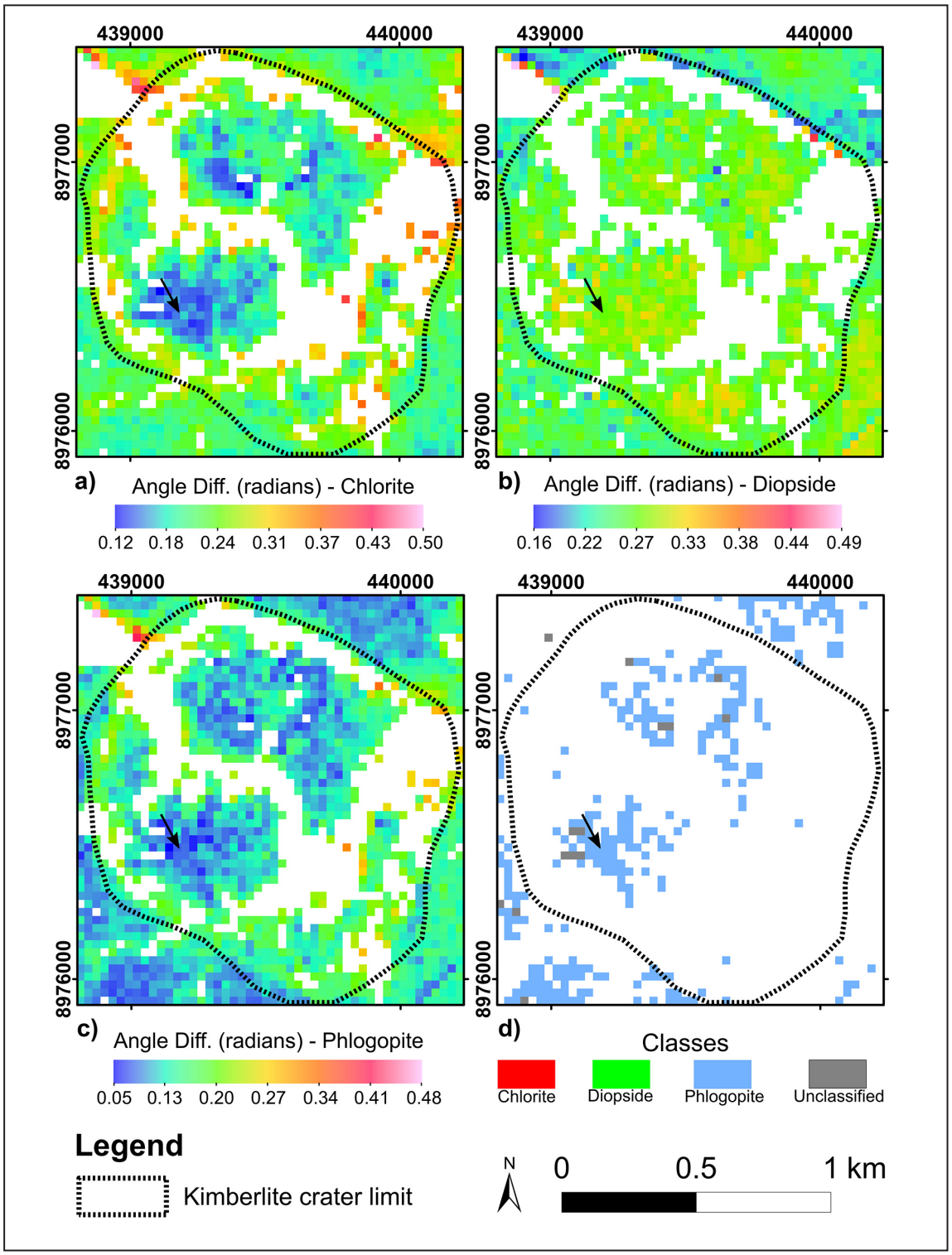

FIGURE 10. Mineral distribution maps derived Spectral Angle Mapping (SAM) methods. The angular difference (in radians) between the VNIR - SWIR image pixel spectra and reference spectra (chlorite, diopside, or phlogopite) are shown in a), b), and c) pictures. d) Classified image.

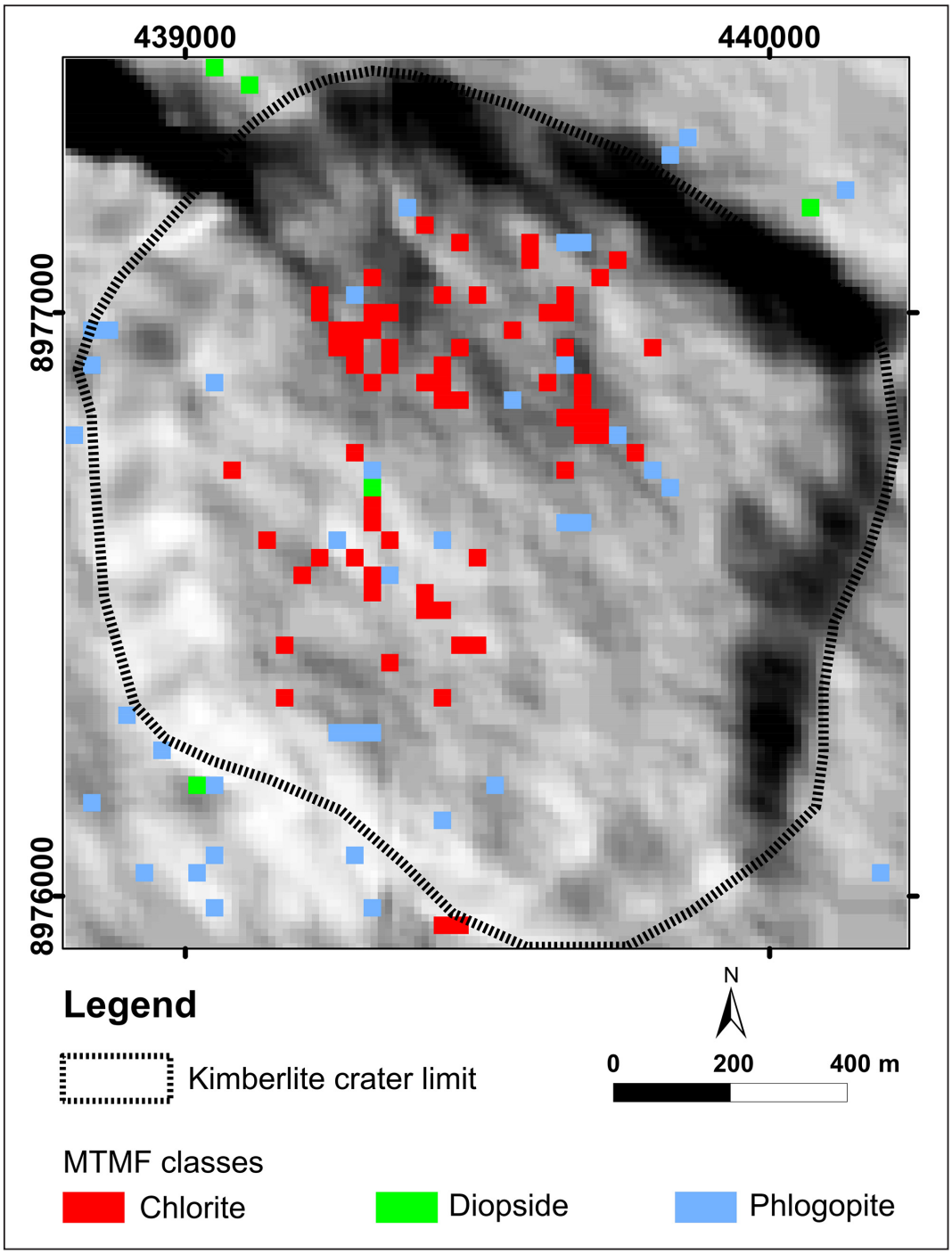

FIGURE 11. Mineral distribution map computed by Mixture Tuned Matched Filtering (MTMF). The red, green, and blue pixels indicate pixels with an MF score > 0.1 and infeasibility < 1.5 for each spectra reference.

spectra. Note that each classified pixel in Figure 10 suggests that the pixel contains 10% or more of the spectral signature of reference spectra (chlorite, diopside, or phlogopite). The chlorite seems predominant within the kimberlite crater, whereas the phlogopite seems to be more spatially scattered. The diopside distribution is very sparse and has very low occurrences, something similar to SAM results. Contrarily to SAM, it is not possible to observe any grouping at the little region where Fe-bearing mafic minerals may have occurred. However, MTMF results also suggested that chlorite, diopside, and phlogopite can be present at Redondão kimberlite intrusion, at least in some proportions.

4. Discussion

Kimberlites are ultramafic rocks with low SiO_2 content when compared to granites. Since K, eTh, and eU concentrations increase with the rise of SiO_2, low radiometric signatures on kimberlites are expected (Galbraith and Saunders 1983; Dickson and Scott 1997; Dentith and Mudge 2014). Similarly, sandstones of Piauí and Pedra de Fogo formations are essentially composed of quartz grains, which are poor in radioelements, such that low airborne radiometric signatures are also expected (Killeen et al. 2015). Therefore, the low radiometric

concentration of the study area can be explained by local geological settings.

Despite radiometric concentrations at the survey area being low, K concentrations seem to be present within the Redondão kimberlite crater in enough quantities to be distinct from surrounding terrain. Commonly, K concentrations at kimberlites are less than Th and U, such that low K concentrations at kimberlite regarding surrounding terrain are commonly expected (Ahrens et al. 1967; Kresten 1974; Paul et al. 1977; Mwenifumbo and Kjarsgaard 1999; Killeen et al. 2015). In order to be detected by airborne surveys, gamma-rays measured at K channel must come from some spatially distributed source(s) within Redondão kimberlite crater. In this sense, one can infer that some K-bearing minerals may be at kimberlite crater. However, the exact identification of this mineral depends on the field work. Here, some insight to explain the K concentration at Redondão kimberlite will be posed.

Based on the available geological information, the origin of K observed at airborne gamma-ray spectrometry can be attributed to two sources: external - that is, K-bearing minerals come from outside the kimberlite crater and, therefore, would not be related to kimberlitic magmatism or its alteration processes, or internal - K-bearing minerals are within the kimberlite crater, and they may be related kimberlitic magmatism or its alteration processes.

Researchers in soil sciences have demonstrated that gamma-ray spectrometry can be a useful tool for mapping important properties of soil, like clay content or grain size (Taylor et al. 2002; Rouze et al. 2017; Mello et al. 2021). Some of these works have reported that alluviums recently deposited along drainage channels may be rich in K- bearing minerals (e.g. K-feldspars) (Bierwirth 1996; Pickup and Marks 2000; Dent et al. 2013). Although this mechanism may be plausible to explain K concentration at KR intrusion, if this were the case, high K concentration would be expected along drainage channels both inside and outside the kimberlite crater.

Alternatively, anomalous isotopic composition and high concentrations of natural elements relative to background values have been reported at Arkhangelskaya kimberlite pipe (Kiselev et al. 2017; Yakovlev 2020). In this case, geological and structural features of kimberlite pipe may have worked as a geochemical barrier, such that radioisotopes carried out by groundwater may have been deposited at kimberlite/host rocks contact zones, yielding a halo of high radiometric concentrations (Yakovlev 2020). Although this mechanism can only be investigated with field work, results reported here suggest that this mechanism cannot explain K concentrations at Redondão kimberlite crater because: i) this mechanism is markedly highlighted by U and Th high concentrations, which do not occur in the Redondão kimberlite area; ii) Even Arkhangelskaya pipe, halos of K concentration are not too evident in relation to Th and U halos; iii) K concentration at Redondão kimberlite crater has a filled circular shape, not a halo; iv) Yet it has not been investigated if gamma-ray associated with this mechanism can be detected by airborne surveys. At Arkhangelskaya kimberlite pipe, an airborne survey was not able to detect any radiometric contrast related to this mechanism (Yakovlev 2020).

Regarding internal origin, K-bearing minerals can be related to several factors, such as hydrothermal alteration, metasomatism, or compositional aspects (Afanasyev et al. 2014; Sparks 2013). In the first two cases, hydrothermal alteration and metasomatism processes do not seem to occur spatially distributed within intrusion (Kaminsky et al. 2009). Moreover, Fp values ($< 1.0 \times 10^{-2}$) within Redondão kimberlite crater support the absence of hydrothermal alteration, as Fp greater than 2.0×10^{-2} would be expected. On the other hand, the Fp increase curve may suggest some processing that can leave a K concentration. For the third case, it is possible that K concentration may be derived from clastic materials derived from kimberlitic rock or related to its emplacement.

Although clastic materials are composed predominantly of altered olivine crystalloclasts at Redondão kimberlite crater, chloritized phlogopite (sometimes only partially) laths occur in minor amounts within Redondão kimberlite, some of which are intergrown with olivine (Kaminsky et al. 2009). Phlogopite is a mineral that can contain up to 9.33 wt% K and can yield radiometric anomalies at micaceous kimberlites with up to 12% phlogopite (Kamara 1981; Dentith and Mudge 2014). In the Redondão kimberlite intrusion, SAM and MTMF maps suggest that phlogopite may be present at Redondão kimberlite crater, but radiometric signals observed at the K channel of the airborne gamma-ray survey are unlikely to be due to only this mineral because sample rocks from Redondão kimberlite contain less than 2% of phlogopite (Kaminsky et al. 2009). Similarly, K-bearing minerals in the groundmass of a few lithoclastic and/or xenogeneic materials (e.g., chloritized mica laths, rare irregular fragments of altered crystalline schist and granitoids, and grains of feldspar) are also unlikely to produce meaningful radiometric concentration alone (Kaminsky et al. 2009). Therefore, it is proposed that gamma-rays at the K channel may come from different sources within Redondão kimberlite crater, including minerals present in lithoclastic and xenogeneic materials and phlogopite.

The presence of clastic materials may also explain some of the results derived from ASTER data. As seen in the previous section, spectral indices from VNIR-SWIR and TIR scenes suggest a little region where Fe-bearing mafic silicate minerals may be present within Redondão kimberlite intrusion. Among the spectral signatures that have been analyzed, SAM maps suggest that chlorite and diopside spectral signatures may be one of the minerals present in the aforementioned small region.

Both chlorite and diopside have absorption features at 0.66 µm, but only chlorite has absorption features at 0.88 µm. Whereas the feature at 0.66 µm is related to Fe^{3+}, 0.88 µm feature may indicate Fe^{3+} electronic transition processing (Bishop 2019). As Redondão kimberlite is an intrusion deepest weathered, 0.66 µm may be related to Fe present in diopside and/or chlorite, whereas 0.88 µm may be related to ultramafic mineral weathered, for instance, Fe contained in chlorite freshly weathered. Alternatively, Fe hydroxyl/oxide at groundmass of few lithoclastic also contributes to explaining these absorption features in the visible region. At the TIR region, a strongly blue-shade as viewed in the small region suggests that spectral features in this area may be related to the fundamental molecular vibration modes of Si - O components into mafic minerals (e.g., diopside and/or chlorite) (Salisbury and D'Aria 1992; Guha and Kumar 2016; Ninomiya and Fu 2019). However, because TIR spectral indices yield low resolution images, it is recommended that new studies be conducted to investigate these TIR spectral features that occur at Redondão kimberlite intrusion.

In addition to absorption features at visible and thermal regions, absorption features at 2.26 µm and 2.33 µm have given

us some interesting insights. It is known that these features in short infrared regions are related to OH vibrational modes (Hunt 1977; Hunt 1979; Hunt and Evarts 1981; Goetz and Rowan 1981; Bishop 2019). The 2.26 µm absorption may suggest the presence of Al^{3+}, whereas the 2.33 µm absorption features may indicate Mg^{3+} (Hunt 1979; Bishop 2019). Both 2.26 µm and 2.33 µm absorption features seen at endmember #1 and #3 are shallower than the reference spectra of chlorite and phlogopite, respectively, but 2.26 µm feature is sharper for endmember #3 than phlogopite. These differences between endmembers derive directly from images and reference spectra from spectral libraries are expected because laboratory spectra are collected in specific conditions that may not reflect real environments (Guha et al. 2012; Guha et al. 2015). However, the fact that the 2.26 µm feature is sharpness for endmember #3 may indicate some hydration process may lead to Al concentration at Redondão kimberlite intrusion. Although this hypothesis is consistent because Redondão kimberlite is a deeply weathered crater, it can only be validated through fieldwork. In this sense, it is recommended that new studies may collect rock spectra to investigate this question.

Spectral differences between endmember and reference spectra may have contributed to reduced SAM and MTFM performance. Additionally, these performances may have been reduced due to the fact that Redondão kimberlite is a strongly weathered crater, which hampers the identification of minerals because soil mixture becomes a more problematic effect. Even so, the good match between endmembers and reference (chlorite, diopside, and phlogopite) spectra shows that the ASA approach may be successfully applied on multispectral data, as demonstrated in previous works (Van der Meer 1995; Van der Meer and De Jong 2000; Rowan and Mars 2003; Pal et al. 2011), even this approach is more suitable for hyperspectral images. In this sense, further research may investigate how hyperspectral sensor images and rock-spectra may improve the sub-pixel classification method and aim to identify other minerals at Redondão kimberlite intrusion.

5. Conclusions

This study was conducted to infer the presence of minerals in the Redondão Kimberlite (Redondão kimberlite) crater from interpretations of airborne gamma-ray spectrometry (AGRS) data and the Advanced Spaceborne Thermal Emission and Reflection Radiometer (ASTER). Using different kind of processing techniques (e.g., K, eTh, and eU concentration maps, K/eTh, K/eU, and eU/eTh ratio maps, K image inverse map, profile analysis for radiometric data; and spectral indexes and mineral distribution and abundance maps for ASTER data), the findings interpreted and reported in this study allow the statement of the following conclusions:

1 - Although the survey area is composed of lithologies marked by low radiometric signatures, K concentrations within Redondão kimberlite intrusion are high enough to be distinct from the surroundings. The sources of K concentrations are unclear, but they are probably composed of different minerals, and phlogopite may be one of them.

2 - At least three spectral signatures of endmembers extracted from ASTER images suggested chlorite, diopside, and phlogopite minerals may be present within Redondão kimberlite crater and its surroundings. However, the lack of rock spectra and the fact that Redondão kimberlite is a deeply weathered crater likely affected the more accurate recognition of these minerals.

3 - The spectral signatures of chlorite, diopside, phlogopite may be derived from clastic materials and products derived from weathered ultramafic minerals, but new studies are recommended to improve the distribution and abundance of these minerals. These new studies may include hyperspectral sensor images and rock-spectra data.

Acknowledgements

The author of this study is grateful to the Brazilian National Agency of Petroleum, Natural Gas and Biofuels and the Remote Sensing and Geophysics Division of the Geological Survey of Brazil for providing the airborne geophysical data that were used in this work. I am also grateful to Monica Mazzini Perrotta for knowledge exchange and discussion. Finally, the author is thankful to Dr. Jefferson Tavares and an anonymous JGSB reviewer for the corrections and observations suggested. Such contributions were essential for improving the manuscript.

Declaration of conflict of interest

The authors declare that they have no known competing financial interests or personal relationships that could have appeared to influence the work reported in this paper.

Data availability

All the data used in this study is in the public domain and can be obtained from the links or websites cited in the text.

Authorship credits

Author	A	B	C	D	E	F
ABS						

A - Study design/Conceptualization **B** - Investigation/Data acquisition
C - Data Interpretation/ Validation **D** - Writing
E - Review/Editing **F** - Supervision/Project administration

References

Afanasyev A.A., Melnik O., Porritt L., Schumacher J.C., Sparks R.S.J. 2014. Hydrothermal alteration kimberlite by convective flows of external water. Contributions to Mineralogy and Petrology, 168(1), 1038. https://doi.org/10.1007/s00410-014-1038-y

Ahrens L.H., Cherry R.D., Erlank A.J. 1967. Observations on the Tn-U relationship in zircons from granitic rocks and from kimberlites. Geochimica et Cosmochimica Acta, 31(12), 2379-2387. https://doi.org/10.1016/0016-7037(67)90009-9

Almeida-Filho R., Castelo Branco R.M.G. 1992. Location of kimberlites using Landsat Thematic Mapper images and aerial photographs: the Redondao diatreme, Brazil. International Journal of Remote Sensing, 13(8), 1449-1457. https://doi.org/10.1080/01431169208904201

Bateson A., Curtiss B. 1996. A method for manual endmember selection and spectral unmixing. Remote Sensing of Environment, 55 (3), 229-243. https://doi.org/10.1016/S0034-4257(95)00177-8

Bierwirth P. 1996. Investigation of airborne gamma-ray images as a rapid mapping tool for soil and land degradation - Wagga Wagga, NSW. Record 1996/022. Canberra City, Australian Geological Survey Organisation, 71 p. Available online at: https://ecat.ga.gov.au/geonetwork/srv/api/records/a05f7892-740e-7506-e044-00144fdd4fa6 / (accessed on 28 August 2023)

Bishop J.L. 2019. Visible and near-infrared reflectance spectroscopy: laboratory spectra of geologic materials. In: Bishop J.L., Bell III J.F., Moersch J.E. (eds.). Remote compositional analysis: techniques for understanding spectroscopy, mineralogy, and geochesmistry of planetary surfaces. Cambridge, Cambridge University Press, p. 68-101. https://doi.org/10.1017/9781316888872.006

Boardman J.W., Kruse F.A., Green R.O. 1995. Mapping target signatures via partial unmixing of AVIRIS data. In: Airborne Visible/Infrared Imaging Spectrometer (AVIRIS) Workshop, 5, 23-26. JPL Publication, 95-1. Available online at: https://ntrs.nasa.gov/api/citations/19950027316/downloads/19950027316.pdf / (accessed on 28 August 2023).

Boardman J.W. 1998. Leveraging the high dimensionality of AVIRIS data for improved sub-pixel target unmixing and rejection of false positives: mixture tuned matched filtering. In: Airborne Visible/Infrared Imaging Spectrometer (AVIRIS) Workshop, 7, 55-56. JPL Publication, 97-21. Pasadena, Jet Propulsion Laboratory. Available online at: https://aviris.jpl.nasa.gov/proceedings/1998_toc.html / (accessed on 28 August 2023).

Castelo Branco R.M.G., Svisero D.P. 1986. Análise de estruturas anelares da região sul do estado do Piauí por meio de produtos de sensoriamento remoto. In: Congresso Brasileiro de Geologia, 34, v. 6, 2973-2983. Available online at: https://repositorio.usp.br/item/000774549 / (accessed on 23 January 2024).

Clark R.N., Gallagher A.J., Swayze G.A. 1990. Material absorption band depth mapping of imaging spectrometer data using a complete band shape least-squares fit with library reference spectra. In: Airborne Visible/Infrared Imaging Spectrometer (AVIRIS) Workshop, 2, 176-186. JPL Publication, 90-54. Pasadena, Jet Propulsion Laboratory. Available online at: https://aviris.jpl.nasa.gov/proceedings/workshops/90_docs/17.PDF / (accessed on 28 August 2023).

Clark R.N., Roush T.L. 1984. Reflectance spectroscopy: quantitative analysis techniques for remote sensing applications. Journal of Geophysical Research, 89(B7), 6329-6340. https://doi.org/10.1029/JB089iB07p06329

Clark R.N., Swayze G.A., Gallagher A. 1992. Mapping the mineralogy and lithology of Canyonlands, Utah with imaging spectrometer data and the multiple spectral feature mapping algorithm. In: Airborne Visible/Infrared Imaging Spectrometer (AVIRIS) Workshop, 3, 11-13. JPL Publication, 92-41. AVIRIS Workshop, v. 1. Pasadena, Jet Propulsion Laboratory. Available online at: https://ntrs.nasa.gov/citations/19940012197 / (accessed on 28 August 2023).

Correia E.A. 1990. Diamantes e kimberlitos do sul e leste da Bacia do Parnaíba (Brasil). PhD Thesis, Faculdade de Ciências, Universidade do Porto, Porto, 184 p. Available online at: http://hdl.handle.net/10216/10222 / (accessed on 28 August 2023).

Dent D.L., MacMillan R.A., Mayr T.L., Chapman W.K., Berch S.M. 2013. Use of airborne gamma radiometrics to infer soil properties for a forested area in British Columbia, Canada. Journal of Ecosystems and Management, 14(1), 1-12. https://doi.org/10.22230/jem.2013v14n1a201

Dentith M., Mudge S.T. 2014. Geophysics for the mineral exploration geoscientist. Cambridge, Cambridge University Press, 516 p. https://doi.org/10.1017/CBO9781139024358

Dickson B.L., Scott K.M. 1997. Interpretation of aerial gamma-ray surveys - adding the geochemical factors. AGSO Journal of Australian Geology and Geophysics, 17(2), 187-200. Available online at: https://pid.geoscience.gov.au/dataset/ga/81502 / (accessed on 23 January 2024).

Drury S.A. 2001. Image interpretation in geology. 3rd ed. Malden, Blackwell Science, xi, 290 p.

Duval J.S. 1983. Composite color images of aerial gamma-ray spectrometric data. Geophysics, 48(6), 722-735. https://doi.org/10.1190/1.1441502

Galbraith J.H., Saunders D.F. 1983. Rock classification by characteristics of aerial gamma-ray measurements. Journal of Geochemical Exploration, 18(1), 49-73. https://doi.org/10.1016/0375-6742(83)90080-8

Girija R.R., Mayappan S. 2019. Mapping of mineral resources and lithological units: a review of remote sensing techniques. International Journal of Image and Data Fusion, 10(2), 79-106. https://doi.org/10.1080/19479832.2019.1589585

Gnojek I., Přichystal A. 1985. A new zinc mineralization detected by airborne gamma-ray spectrometry in northern Moravia (Czechoslovakia). Geoexploration, 23(4), 491-502. https://doi.org/10.1016/0016-7142(85)90076-6

Goetz A.F.H., Rowan L.C. 1981. Geologic remote sensing. Science, 211(4484), 781-791. https://doi.org/10.1126/science.211.4484.781

Green A.A., Berman M., Switzer P., Craig M.D. 1988. A transformation for ordering multispectral data in terms of image quality with implications for noise removal. IEEE Transaction on Geoscience and Remote Sensing, 26(1), 65-74. https://doi.org/10.1109/36.3001

Guha A., Rao D.A., Ravi S., Kumar K.V., Rao E.N.D. 2012. Analysis of the potential of kimberlite rock spectra as spectral end member using samples from Narayanpet Kimberlite Field, Andhra Pradesh. Current Science, 103(9), 1096-1104. Available online at: http://www.jstor.org/stable/24089080 / (accessed on 23 January 2024).

Guha A., Kumar K.V., Ravi S., Rao E.N.D. 2015. Reflectance spectropy of kimberlites – in parts of Dharwar Craton, India. Arabian Journal of Geosciences, 8(11), 9373-9388. https://doi.org/10.1007/s12517-015-1850-3

Guha A., Kumar K.V. 2016. New ASTER derived thermal indices to delineate mineralogy of different granitoids of an Archaean Craton and analysis of their potentials with reference to Ninomiya's indices for delineating quartz and mafic minerals of granitoids – an analysis in Dharwar Craton, India. Ore Geology Reviews, 74, 76-87. https://doi.org/10.1016/j.oregeorev.2015.10.033

Hunt G.R. 1977. Spectral signatures of particulate minerals in the visible and near infrared. Geophysics, 42(3), 501-513. https://doi.org/10.1190/1.1440721

Hunt G.R. 1979. Near-infrared (1.3–2.4 μm) spectra of alteration minerals – potential for use in remote sensing. Geophysics, 44(12), 1974-1986. https://doi.org/10.1190/1.1440951

Hunt G.R., Evarts R.C. 1981. The use of near-infrared spectroscopy to determine the degree of serpentinization of ultramafic rocks. Geophysics, 46(3), 316-321. https://doi.org/10.1190/1.1441202

IAEA. 2003. Guidelines for radioelement mapping using gamma-ray spectrometry data. Vienna, Austria, IAEA, 173 p. Available online at: https://www.iaea.org/publications/6746/guidelines-for-radioelement-mapping-using-gamma-ray-spectrometry-data / (accessed on 24 January 2024).

Jelsma H., Barnett W., Richards S., Lister G. 2009. Tectonic setting of kimberlites. Lithos, 112(supl.), 155-165. https://doi.org/10.1016/j.lithos.2009.06.030

Kalinowski A., Oliver S. (comp.). 2004. ASTER mineral index processing manual. Canberra, Geoscience Australia, 36 p. Available online at: https://ecat.ga.gov.au/geonetwork/srv/eng/catalog.search#/metadata/67973 / (accessed on 28 August 2023).

Kamara A.Y.S. 1981. Review: geophysical methods for kimberlite, prospecting. Exploration Geophysics, 12(3), 43-51. https://doi.org/10.1071/EG981043

Kaminsky F.V., Sablukov S.M., Sablukova L.I., Zakharchenko O.D. 2009. The Fazenda Largo off-craton kimberlites of Piauí State, Brazil. Journal of South American Earth Sciences, 28(3), 288-303. https://doi.org/10.1016/j.jsames.2009.06.003

Kaminski V., Oldenburg D. 2012. The geophysical study of Drybones kimberlite using 3D Time Domain EM Inversion and 3D ZTEM inversion algorithms. ASEG Extended Abstracts, 2012(1), 1-4. Geophysical Conference, 22. https://doi.org/10.1071/ASEG2012ab324

Khan S.D., Mahmood K. 2008. The application of remote sensing techniques to the study of ophiolites. Earth-Science Reviews, 89(3-4), 135-143. https://doi.org/10.1016/j.earscirev.2008.04.004

Killeen P.G., Mwenifumbo C.J., Ford K.L. 2015. 11.14 - Tools and techniques: radiometric methods. In: G. Scubert (ed.). Treatise on Geophysics. 2nd ed. Amsterdam, Elsevier, v. 11, 447-524. https://doi.org/10.1016/B978-0-444-53802-4.00209-8

Kiselev G.P., Yakovlev E.Y., Druzhinin S.V., Galkin A.S. 2017. Distribution of radioactive isotopes in rock and ore of Arkhangelskaya pipe from the Arkhangelsk diamond province. Geology of Ore Deposits, 59(5), 391-406. https://doi.org/10.1134/S1075701517050014

Kokaly R.F., Clark R.N., Swayze G.A., Livo K.E., Hoefen T.M., Pearson N.C., Wise R.A., Benzel W.M., Lowers H.A., Driscoll R.L., Klein A.J. 2017. USGS spectral library version 7. Data Series, 1035. Reston, VA, U.S. Geological Survey, 61 p. https://doi.org/10.3133/ds1035

Kresten P. 1974. Uranium in kimberlites and associated rocks, with special reference to Lesotho occurrences. Lithos, 7(3), 171-180. https://doi.org/10.1016/S0024-4937(74)80001-0

Kruse F.A., Lefkoff A.B., Boardman J.W., Heidebrecht K.B., Shapiro A.T., Barloon P.J., Goetz A.F.H. 1993. The Spectral Image Processing System (SIPS)–interactive visualization and analysis of imaging spectrometer data. Remote Sensing of Environment, 44(2-3), 145-163. https://doi.org/10.1016/0034-4257(93)90013-N

Lima M.I.C., Monteiro N., Silva L.D., Marinho D. 1990. Identificação de morfoestruturas anômalas na porção centro-oriental da bacia do Maranhão (Brasil), através de imagens SLAR e Landsat-TM. In: Simpósio Brasileiro de Sensoriamento Remoto, 6, 663-670.

LP DAAC. 2020. AST_L1T v003: ASTER level 1 precision terrain corrected registered At-sensor radiance. Sioux Falls, SD, Land Processes DAAC, data set. https://doi.org/10.5067/ASTER/AST_L1T.003

Macnae J. 1995. Applications of geophysics for the detection and exploration of kimberlites and lamproites. Journal of Geochemical Exploration, 53(1-3), 213-243. https://doi.org/10.1016/0375-6742(94)00057-I

Matende K., Mickus K. 2021. Magnetic and gravity investigation of kimberlites in north-central Botswana. Geophysics, 86(2), B67-B78. https://doi.org/10.1190/geo2020-0450.1

Marques R.P., Kassab Jr F., Molina E.C., Andrade F.A.R. (org.). 2007. Levantamentos aerogeofísicos para a identificação de áreas com ocorrência potencial de petróleo e gás na Bacia do Parnaíba. Tomo II: área Parnaíba, aerolevantamento magnético e gamaespectrométrico. São Paulo, ANP, USP, v. I.A, 109 p.

Mazer A.S., Martin M., Lee M., Solomon J.E. 1988. Image processing software for imaging spectrometry data analysis. Remote Sensing of Environment, 24(1), 201-210. https://doi.org/10.1016/0034-4257(88)90012-0

Mello D.C., Demattê J.A.M., Mello F.A.O., Poppiel R.R., Silvero N.E.Q., Safanelli J.L., Souza A.B., Di Raimo L.A.D.L., Rizzo R., Resende M.E.B., Schaefer C.E.G.R. 2021. Applied gamma-ray spectrometry for evaluating tropical soil processes and attributes. Geoderma, 381, 114736. https://doi.org/10.1016/j.geoderma.2020.114736

Menezes P.T.L., La Terra E.F. 2011. 3D magnetic interpretation of the Regis kimberlite pipe, Minas Gerais, Brazil. Near Surface Geophysics, 9(4), 331-338. https://doi.org/10.3997/1873-0604.2011005

Mitchell R.H. 2021. Potassic alkaline rocks: leucitites, lamproites, and kimberlites. In: Alderton D., Elias S.A. (eds.). Encyclopedia of geology. 2nd. ed. London, Academic Press, p. 215-239. https://doi.org/10.1016/B978-0-12-409548-9.12482-0

Mwenifumbo C.J., Kjarsgaard B.A. 1999. Gamma-ray logging and radioelement distribution in the Fort a la Corne kimberlite pipe 169. Exploration and Mining Geology, 8(1-2), 137-174. Available online at: https://pubs.geoscienceworld.org/cim/emg/article/8/1-2/137/61162/Gamma-ray-logging-and-radioelement-distribution-in / (accessed on 26 January 2024).

Ninomiya Y., Fu B. 2019. Thermal infrared multispectral remote sensing of lithology and mineralogy based on spectral properties of materials. Ore Geology Reviews, 108, 54-72. https://doi.org/10.1016/j.oregeorev.2018.03.012

Nndanduleni M., Tessema A. 2021. Identification of potential targets for kimberlite exploration using satellite imagery and map combination approach in the Lesotho Kimberlite Province. Ore Geology Reviews, 132, 104001. https://doi.org/10.1016/j.oregeorev.2021.104001

NV5 Geospatial. 2023a. Spectral feature fitting. Available online at: https://www.nv5geospatialsoftware.com/docs/SpectralFeatureFitting.html / (accessed on 29 January 2024).

NV5 Geospatial. 2023b. Binary encoding. Available online at: https://www.nv5geospatialsoftware.com/docs/BinaryEncoding.html / (accessed on 29 January 2024).

Oliveira J.C. 1998. Recursos gemológicos dos estados do Piauí e Maranhão. Informe de Recursos Minerais, Série Pedras Preciosas, 4. Teresina, CPRM, 36 p. Available online at: https://rigeo.sgb.gov.br/handle/doc/1629 / (accessed on 28 August 2023).

Otsu N. 1979. A threshold selection method from gray-level histograms. IEEE Transactions on Systems, Man, and Cybernetics, 9(1), 62-66. https://doi.org/10.1109/TSMC.1979.4310076

Pal S.K., Majumdar T.J., Bhattacharya A.K., Bhattacharyya R. 2011. Utilization of Landsat ETM+ data for mineral-occurrences mapping over Dalma and Dhanjori, Jhakhand, India: an advanced spectral analysis approach. International Journal of Remote Sensing, 32(14), 4023-4040. https://doi.org/10.1080/01431161.2010.484430

Paul D.K., Gale N.H., Harris P.G. 1977. Uranium and thorium abundances in Indian kimberlites. Geochimica et Cosmochimica Acta, 41(2), 335-339. https://doi.org/10.1016/0016-7037(77)90241-1

Pettit W. 2009. Geophysical signatures of some recently discovered large (>40ha) kimberlite pipes on the Alto Cuilo concession in northeastern Angola. Lithos, 112(supl. 1), 106-115. https://doi.org/10.1016/j.lithos.2009.05.046

Pickup G., Marks A. 2000. Identifying large-scale erosion and deposition processes from airborne gamma radiometrics and digital elevation models in a weathered landscape. Earth Surface Processes and Landforms, 25(5), 535-557. https://doi.org/10.1002/(SICI)1096-9837(200005)25:5<535::AID-ESP91>3.0.CO;2-N

Pour A.B., Hashim M., Pournamdari M. 2015.Chromitite prospecting using Landsat TM and ASTER remote sensing data. In: ISPRS Annals of the Photogrammetry, Remote Sensing and Spatial Information Sciences, II-2/W2, 99-103. https://doi.org/10.5194/isprsannals-II-2-W2-99-2015

Reed L.E., Witherly K.E. 2007. 50 years of kimberlite geophysics, a review. In: Exploration 07: Decennial International Conference on Mineral Exploration, 5, 679-689. Available online at: https://www.911metallurgist.com/blog/wp-content/uploads/2015/10/50-Years-of-Kimberlite-Geophysics-A-Review.pdf / (accessed on 28 August 2023).

Rouze G.S., Morgan C.L.S., McBratney A.B. 2017. Understanding the utility of aerial gamma radiometrics for mapping soil properties through proximal gamma surveys. Geoderma, 289, 185-195. https://doi.org/10.1016/j.geoderma.2016.12.004

Rowan L.C., Mars J.C. 2003. Lithologic mapping in the Mountain Pass, California area using Advanced Spaceborne Thermal Emission and Reflection Radiometer (ASTER) data. Remote Sensing of Environment, 84(3), 350-366. https://doi.org/10.1016/S0034-4257(02)00127-X

Salisbury J.W., D'Aria D.M. 1992. Emissivity of terrestrial materials in the 8–14 µm atmospheric window. Remote Sensing of Environment, 42(2), 83-106. https://doi.org/10.1016/0034-4257(92)90092-X

Silveira F.V., Neto I.C., Cunha L.M. 2018. Projeto Diamante Brasil. In: Simpósio Brasileiro de Geologia do Diamante, 7.

Sparks R.S.J. 2013. Kimberlite volcanism. Annual Review of Earth and Planetary Sciences, 41, 497-528. https://doi.org/10.1146/annurev-earth-042711-105252

Svisero D.P., Meyer H.O.A., Tsai H.-M. 1977. Kimberlite minerals from Vargem (Minas Gerais) and Redondão (Piauí) diatremes, Brazil; and garnet lherzolite xenolith from Redondão diatreme. Revista Brasileira de Geociências, 7(1), 1-13. Available online at: https://repositorio.usp.br/item/002162263 / (accessed on 26 January 2024).

Svisero D.P. 1995. Distribution and origin of diamonds in Brazil: an overview. Journal of Geodynamics, 20(4), 493-514. https://doi.org/10.1016/0264-3707(95)00017-4

Tappe S., Smart K., Torsvik T., Massuyeau M., Wit M. 2018. Geodynamics of kimberlites on a cooling Earth: clues to plate tectonic evolution and deep volatile cycles. Earth and Planetary Science Letters, 484, 1-14. https://doi.org/10.1016/j.epsl.2017.12.013

Taylor M.J., Smettem K., Pracilio G., Verboom W. 2002. Relationships between soil properties and high-resolution radiometrics, central eastern wheatbelt, western Australia. Exploration Geophysics, 33(2), 95-102. https://doi.org/10.1071/EG02095

Tessema A., Nefele N., Sebake D. 2012. The use of high-resolution airborne magnetic, ASTER and Landsat 7 ETM+ images for identification of kimberlite pipes in the northwestern Free State Province, South Africa. International Journal of Remote Sensing, 33(14), 4356-4373. https://doi.org/10.1080/01431161.2011.640960

Torsvik T.H., Burke K., Steinberger B., Webb S.J., Ashwal L.D. 2010. Diamonds sampled by plumes from the core–mantle boundary. Nature, 466(7304), 352-357. https://doi.org/10.1038/nature09216

Van Der Meer F. 1995. Spectral unmixing of Landsat Thematic Mapper data. International Journal of Remote Sensing, 16(16), 3189-3194. https://doi.org/10.1080/01431169508954622

Van Der Meer F., De Jong S.M. 2000. Improving the results of spectral unmixing of Landsat Thematic Mapper imagery by enhancing the orthogonality of end-members. International Journal of Remote Sensing, 21(15), 2781-2797. https://doi.org/10.1080/01431160050121249

Yamaguchi Y., Kahle A.B., Tsu H., Kawakami T., Pniel M. 1998. Overview of Advanced Spaceborne Thermal Emission and Reflection Radiometer (ASTER). IEEE Transactions on Geoscience and Remote Sensing, 36(4), 1062-1071. https://doi.org/10.1109/36.700991

Yakovlev E.Y. 2020. Features of radioactive element distribution within the Arkhangelsk diamondiferous province: possible directions for development of isotope – radiogeochemical methods for kimberlite prospecting in complex landscape – geology and climate conditions of the subarctic zone. Geochemistry: Exploration, Environment, Analysis, 20(3), 269-279. https://doi.org/10.1144/geochem2019-023

Woodhead J., Hergt J., Giuliani A., Maas R., Phillips D., Pearson D.G., Nowell G. 2019. Kimberlites reveal 2.5-billion-year evolution of a deep, isolated mantle reservoir. Nature, 573(7775), 578-581. https://doi.org/10.1038/s41586-019-1574-8